ChemPubSoc Europe

DOI: 10.1002/celc.201901939

CHEMELECTROCHEM Articles

Electroless Nanoplating of Pd–Pt Alloy Nanotube Networks: Catalysts with Full Compositional Control for the Methanol Oxidation Reaction

Tobias Stohr,* Angelina Fischer, Falk Muench, Markus Antoni, Stephan Wollstadt, Christian Lohaus, Ulrike Kunz, Oliver Clemens, Andreas Klein, and Wolfgang Ensinger[a]

Due to its simplicity, flexibility and conformity, electroless plating presents itself as an attractive route towards functional metal nanostructures. Despite the importance for creating multimetallic materials with enhanced properties, the complex interactions between the components in electroless plating baths make alloy formations a challenging objective. In this work, we outline an electroless plating strategy fabricating Pd–Pt alloy nanomaterials, which is based on arbitrarily miscible plating baths for the individual metals. To demonstrate the excellent nanoscale conformity and homogeneity of our plating system, we apply it to ion track-etched polymer templates with large inner surfaces as ambitious substrates, resulting in the formation of 3D free-standing Pd_xPt_{100-x}-nanotube-networks (NTNWs). Based on the electro-oxidation of methanol as a model reaction, we utilize the compositional freedom provided by our syntheses for optimizing the catalytic performance of our metal NTNWs, which heavily depends on the Pd–Pt ratio. Within our system, the highest surface normalized activity was found for the $Pd_{20}Pt_{80}$ NTNW, reaching more than a two-fold increase of the peak current density in comparison to pure Pt. Overall, our reaction system provides a versatile toolkit for fabricating intricate Pd–Pt nanostructures of arbitrary elemental composition, and constitutes a starting point for designing new electroless alloy plating baths.

1. Introduction

Metallic nanostructures are of great interest because of their large variety of catalytic,[1–12] magnetic,[13,14] mechanical or optical properties.[15,16] By utilizing alloys instead of single metals, the functionality of such nanostructures can be altered and enhanced. Within multimetallic systems, synergistic effects can be achieved.[17–25] For instance, compared to their constituents, bimetallic Pd–Pt nanomaterials can offer improved activity in catalytic applications.[22–25] Aside the composition, the shape and size of nanostructures represent important factors in determining their properties. In this regard, metal nanotubes (NTs) as one-dimensional, hollow nanoobjects frequently outperform more conventional morphologies, such as nanoparticles (NPs).[1,2,9] Besides synthetic approaches for creating Pd catalysts with distinct architecture,[26–28] the implementation of Pd in alloyed Pt-nanotube networks (NTNWs) represents an interesting structure for catalysis applications, because we can combine compositional, synergistic effects between Pd and Pt with the general advantages of NTNWs: NTNWs are free-standing, open-porous structures that consist of NPs as interconnected building blocks.[1,2,29–31] Therefore, NTNWs combine the advantages of NPs, namely functionality and high surface area, with the advantages of a network structure that is stable, convenient to handle, efficient in mass transfer and providing continuous conduction pathways.[1,2,29–31] Optimized NT catalysts exhibit a high density of easily accessible active sites and are more durable as compared to carbon-supported nanoparticle catalysts.[1,2,29–31]

Alloying Pt with transition metals represents a major strategy for enhancing its activity *via* compositional effects that result from bifunctionality and the alloy's electronic system, dependent on the second alloyed metal.[32–34] Pt-based bimetallic nanomaterials (e.g., with Cu, Ir, Ni, Pd, Ru) have been in the focus of catalysis and energy research.[32–34,49–51] For instance, Pt–Ru constitutes a well-established, high-performing material combination for the methanol oxidation reaction (MOR).[50,51] Since Pt has already been successfully combined with Ru to enhance the MOR performance of electrolessly plated nanotube catalysts,[5] in this work, we focus on exploring Pd–Pt as a new bimetallic system.

Due to the high symmetry of metal crystal lattices, it is difficult to directly grow NTs as hollow, highly anisotropic structures of large surface area. This challenge is commonly overcome by using template-guided metal depositions.[1,2,6–9,12,35–38] The conventional electroless plating of macroscopic template components advanced to metal deposition onto nanostructured templates. For instance, it is possible to reliably and independently control the density, diameter,

[a] T. Stohr, A. Fischer, Dr. F. Muench, M. Antoni, S. Wollstadt, C. Lohaus, U. Kunz, Prof. Dr. O. Clemens, Prof. Dr. A. Klein, Prof. Dr. W. Ensinger
Department of Materials and Earth Sciences
Technische Universität Darmstadt
Alarich-Weiß-Str. 2
64287 Darmstadt, Germany
E-mail: stohr@ma.tu-darmstadt.de

Supporting information for this article is available on the WWW under https://doi.org/10.1002/celc.201901939

interconnectivity and shape of the template pores and thus the morphology of the resulting NTs through ion-track-etching technology.[1,2] The amount of deposited metal can be easily adjusted by the plating time. The consequent product morphologies range from isolated particles,[12,30] over NTs of adjustable wall thickness,[1,2,12] to completely filled nanochannels, resulting in the formation of nanowires.[30] In this work, we propose a strategy to adjust the material's composition through a bimetallic electroless plating procedure on the basis of the growing knowledge about monometallic electroless plating on the nanoscale.[1,2,7,8]

Among various synthesis routes to prepare Pd–Pt catalysts for catalytic applications,[39–44] electroless plating represents a facile solution deposition method with excellent scalability and conformity, making it a very promising tool for nanofabrication.[1,2,6–9,12,35–38] In contrast to other deposition methods such as electrodeposition or evaporation, it requires neither complex instrumentation nor specific template properties (e.g., conductivity or heat-resistance). Furthermore, due to its excellent conformity, it is compatible with complex shaped substrates and recessed surfaces. Compositional control can be achieved by co-deposition of different metals, as it is known for the mechanistically related electrodeposition technique.[45–47] Generally, compared to electrodeposition, the electroless alloy deposition is more challenging because of the increased complexity of the plating solutions, which have to fulfill diverse reactivity requirements. First, the metal deposition potential is reached via autocatalytic oxidation of a reducing agent on the evolving metallic deposit and cannot be directly and externally controlled, as it is possible in electrodeposition. Second, the metal reduction reaction has to strike a difficult balance between reactivity and stability of the present metal ions, in order to achieve a metastable deposition condition. A large number of factors contribute to the system's reactivity, including the pH value, metal ion complexation, temperature, choice of reducing agent, and reagent concentrations. As a result of these complexities, even chemically related elements like silver and gold vary tremendously in their respective plating conditions.[12,48]

The electroless plating of multi-metal systems adds further requirements to the plating bath's reactivity, making the realization of such systems even more demanding. Here, each possible combination of the present metal complexes and reducing agent(s) must simultaneously fulfill the metastability criterion, notably under the same global conditions (i.e., composition, temperature and pH value). Additional problems arise from the interference of components in extended plating baths. One metal cation could form a poorly soluble compound with the ligand used to stabilize another, causing precipitation. If an alloy is deposited, its catalytic activity towards the oxidation of the reducing agent will differ from the monometallic deposits, which can dramatically affect the mechanism of the heterogeneously autocatalyzed deposition reaction. Lastly, to allow for the inclusion of all involved metals into the deposit in notable quantities, both metal deposition rates must be similar and ideally tunable, which is an important requirement for establishing compositional control.

A notable exception is the trimetallic system of nickel–cobalt–iron alloys, including boron or phosphorous, where compatible ligands, reducing agents, similar pH value and temperature requirements for the individual metal baths lead to comparable activities and reduction potentials.[29]

Our strategy for co-depositing noble metal alloys aimed at establishing similarly compatible reaction conditions for the involved metals Pd and Pt: We designed electroless plating baths for Pd and Pt which both utilize the same reducing agent (hydrazine), can be operated under identical conditions, do not exhibit fatal component interferences and possess comparable deposition rates. At this point, conformal nanoscale alloy deposits of fully tunable composition can be plated on complex shaped substrates by simply immersing them into plating baths containing different ratios of the individual Pd and Pt deposition solutions.

As an important example of strongly composition-dependent catalytic reactions,[49–51] we chose the MOR to demonstrate the capabilities of our alloy nanoplating system. The MOR is a very interesting reaction for the application in direct fuel cells:[1,33–34] Alongside the high energy density of methanol, its production cost is low and its impact on air quality is lower compared to other alternative fuels due to less reactive exhaust emissions.[52]

2. Results and Discussion

2.1. Synthesis Design

In order to start electroless plating on substrates without intrinsic catalytic activity (such as the polymer templates employed here), metal seeds are commonly introduced to the substrate surface via activation reactions: By alternately immersing the template in solutions of Sn(II) and Pd(II) salts, Pd NPs are formed according to Equations (1) and (2):

$$Sn_{aq}(II) \rightarrow Sn_{ads}(II) \quad (1)$$

$$Sn_{ads}(II) + Pd_{aq}(II) \rightarrow Sn_{ads}(IV) + Pd_{ads}(0) \quad (2)$$

The driving force of this reaction is the difference in the electrochemical reduction potentials between the two metals. Residues of ionic Sn can be found on the template's surface, like it has been analyzed in previous works.[1,2,29] By applying sensitization [Eq. (1)] and activation [Eq. (2)] alternately, the template's surface is covered with Pd NPs, whose amount can be controlled by the number of seeding cycles. The NP seeds initiate the electroless plating reaction, which at later stages advances autocatalytically due to the catalytic qualities of the metal deposit (Figure 1). From our experience, the Pd seeds play a marginal role for the overall stoichiometry: They only cover a small fraction of the nanotubes' surface and shrink or dissolve under subtle galvanic exchange during electroless plating,[53] making them hard to detect for most bulk analysis techniques. EDS measurements did not show any Pd content in the Pd_0Pt_{100} NTNW sample, suggesting that the Pd seeding only

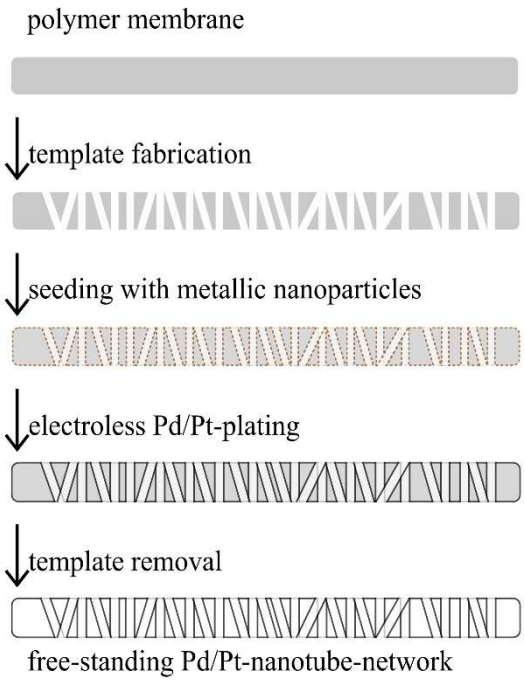

Figure 1. Outlined synthesis route towards the fabrication of free-standing metallic NTs.

affects the catalyst performance to a minor degree. Furthermore, since the same Pd NP seeding was applied to all Pd–Pt NTNW catalysts, the seeding influence is systematic and should not override the compositional impact defined by the metal deposition.

Pd NPs show good activity for oxidizing the utilized reducing agent hydrazine, which is employed for both our electroless Pd and Pt plating reaction. Hydrazine generally undergoes intermediate oxidation states, e.g. diimide, whereas the overall oxidation mechanism of hydrazine in the utilized plating baths can be described by the following equation [Eq. (3)]:[54]

$$N_2H_4 + 4OH^- \leftrightarrow N_2 + 4H_2O + 4e^- \qquad E^0 = -1.16\,V \qquad (3)$$

The electrons accumulating on the NP seeds or the metal deposit due to hydrazine oxidation then reduce the Pd^{2+} and Pt^{4+} species in the plating bath to elemental metal [Eqs. (4)-(6)]:[55,56]

$$Pd^{2+} + 2e^- \leftrightarrow Pd^0 \qquad E^0 = 0.951\,V \qquad (4)$$

$$Pt^{4+} + 2e^- \leftrightarrow Pt^{2+} \qquad E^0 = 1.18\,V \qquad (5)$$

$$Pt^{2+} + 2e^- \leftrightarrow Pt^0 \qquad E^0 = 0.68\,V \qquad (6)$$

Previous studies show that, aside from elemental Pt, the Pt^{4+} precursor complexes are also reduced to Pt^{2+} in the reaction solution.[5] It should be noted that the actual reduction potentials in our system are affected by the concentration and complexation of the metal ions, and thus deviate from the above-mentioned values.

Electroless plating results in moderate plating speeds in the range of 25–50 nm h^{-1} at 80 °C for both Pd and Pt and produces homogeneous deposit thicknesses throughout the template. The plating speeds were calculated by dividing the deposit thickness by the deposition time, after assuming a constant deposition rate. Many factors complicate this analysis: Before plating proceeds continuously, induction periods of variable timespans must pass through which the deposition potential is reached on the catalyst.[57] In the case of nanoparticle-seeded inactive substrates (like in our case), the catalytically active surface increases greatly during the initial stages of deposition. Spatial and temporal fluctuations of the material and reagent concentrations within the template's complex 3D architecture can cause inhomogeneities, such as thicker metal films in the vicinity of the pore openings.[58] Thus, our ex situ plating rate analysis provides a straightforward way of proving the comparable plating rates of the parent metals, which is a requisite for fully tunable electroless alloy deposition, but it cannot deliver precise and time-resolved information about the reaction.

The plating baths are designed to prevent homogeneous nucleation, resulting in the precipitation of metal powder, which can subsequently accumulate on the template surfaces, causing pore clogging.[59] By mixing the fully compatible Pd and Pt plating baths in different ratios, free-standing NT-networks of freely adjustable composition can be obtained, including the monometallic confines as well as the entire alloy system (Figure 2). After the electroless plating procedure, the previously whitish, semi-transparent template is covered with a shiny grey-metallic film that is typical for both Pd and Pt. Removing the metal film on the top and bottom sides of the template membrane with abrasive paper allows looking into the interior of the template, which then appears dark due to light attenuation through scattering events between the large number of interfaces in the polycarbonate-embedded nanonetwork. Due to the full interconnection of nanochannels, metal NTNWs are characterized by continuous conduction paths and represent an important class of 3D nanostructured metal materials which combine good electrical conductivity with high porosity, rendering them promising for electrochemical applications, such as sensing and catalysis.[2]

Pd/Pt nanostructures are employed for catalyzing a large variety of chemical reactions. We chose the methanol electrooxidation, which is of tremendous interest for fuel cell applications,[1,5,9,18,21,35–38] as a model reaction for investigating the composition-dependent catalytic properties of our NT networks. Pt catalysts employed in the oxidation of small organic molecules are susceptible to poisoning through intermediates such as CO, which strongly bind to the active sites. This CO-poisoning could be mitigated by the addition of Pd:[35–38] Compared to commercial Pt/C, $Pd_{40}Pt_{60}$ concave nanocubes (NCs) showed a 4.6 times higher specific mass activity for the MOR and a better tolerance towards CO-poisoning which could be caused by synergistic effects between Pd and Pt besides their facetted surface structure.[32] Other shapes of

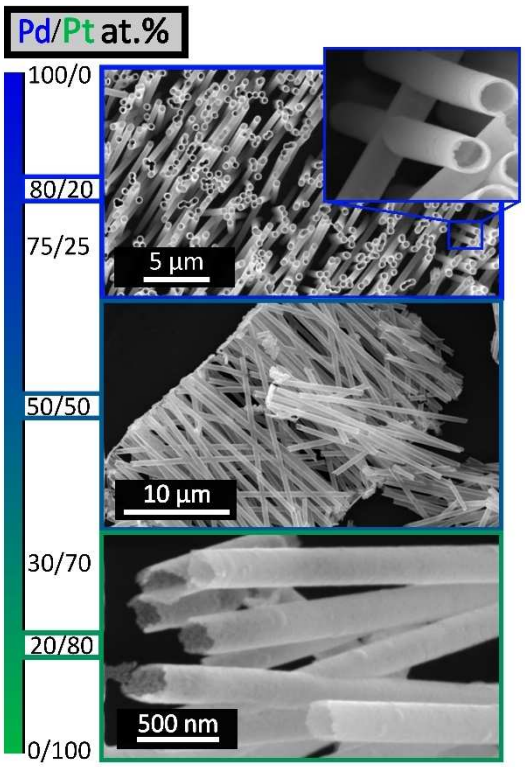

Figure 2. Schematic illustration of the bimetallic Pd/Pt-NT-spectrum enabled by the flexible synthesis route through adjusting the volume fractions of electroless Pd and Pt plating baths.

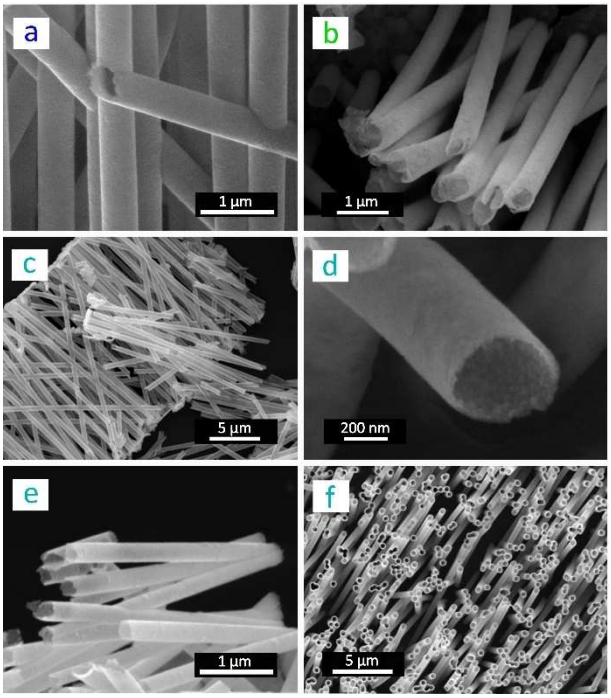

Figure 3. SEM-images of: (a): Pd NTNW; (b): Pt NTNW; (c): $Pd_{50}Pt_{50}$ NTNW; (d): opening of a $Pd_{50}Pt_{50}$-NT; (e): $Pd_{20}Pt_{80}$ NTNW; (f): $Pd_{80}Pt_{80}$ NTNW.

nanostructures, for example Pt-on-Pd nano-dendrites, confirm the promoting role of Pd in the presence of Pt compared to commercial catalysts with respect to mass activity in the MOR.[33] There is evidence for Pd–Pt synergy in other catalytic systems, for example a preferred direct oxidation of formic acid on Pd in a Pt–Pd alloy surface, circumventing CO-poisoning.[34]

In the following, we want to show how the general strategy of template-assisted electroless plating of 3D nanostructured materials, which so far has been focusing on the deposition of single metals, can be augmented by compositional control to improve the catalytic performance. Overall, our aim is to maximize synergetic effects between Pd and Pt within our MOR model reaction by varying the bimetallic composition of our NTNWs.

2.2. Structural and Compositional Analysis of the Nano-Networks

SEM measurements confirmed the successful deposition of conformal nanoscale films, resulting in the formation of well-defined NTs through the full spectrum of Pd/Pt ratios (Pd_0Pt_{100}, $Pd_{20}Pt_{80}$, $Pd_{30}Pt_{70}$, $Pd_{50}Pt_{50}$, $Pd_{75}Pt_{25}$, $Pd_{80}Pt_{20}$, $Pd_{100}Pt_0$). Generally, the deposited material is enriched in Pt as compared to the electrolyte, in agreement with the more noble character of this metal. Figure 3 contains SEM-images of the two system confining monometallic NTs. The film is very smooth on the outer NT wall surface, reflecting the even surface of the nanochannels inside the polymer template. Figure 3 (c) depicts the $Pd_{50}Pt_{50}$ NTs, which is composed of individual NTs consistently interconnected through the entire template thickness of 20 µm. Figure 3 (d) shows the same sample at higher magnification. With an observed diameter of 400 nm, the NTs match the nominal pore dimensions provided by the supplier. The inner NT wall surface is rougher as compared to the smooth outer wall, indicating the structural evolution of the deposit on the channel wall. Figure 3 (e) and (f) feature two bimetallic, Pt and Pd-rich samples, respectively ($Pd_{80}Pt_{20}$/$Pd_{20}Pt_{80}$). The aspect-ratio for NTs with perpendicular orientation respective to the membrane's surface is the length L of the NTs divided by their diameter d [Eq. (7)]:

$$L/d = 20\ \mu m/0.4\ \mu m = 50 \tag{7}$$

The length of tilted NTs in the network exceeds the template thickness, resulting in aspect-ratios up to 100. Furthermore, the synthesis route has reliable control over a wide range of associated variables, like wall thickness, diameter and length of the NTs. This can be achieved by simple means, such as changing the polymer template dimensions (thickness, pore diameter) and varying the deposition time.

TEM was used to gain a more thorough understanding of the product nanostructure. Figure 4 displays a cross section through a NTNW. The deposit appears homogeneous throughout all pores, corroborating the SEM results. Pores can overlap (Figure 4(a)), resulting in the appearance of intersections that are typical for NTNWs. Figure 4b shows the cross section

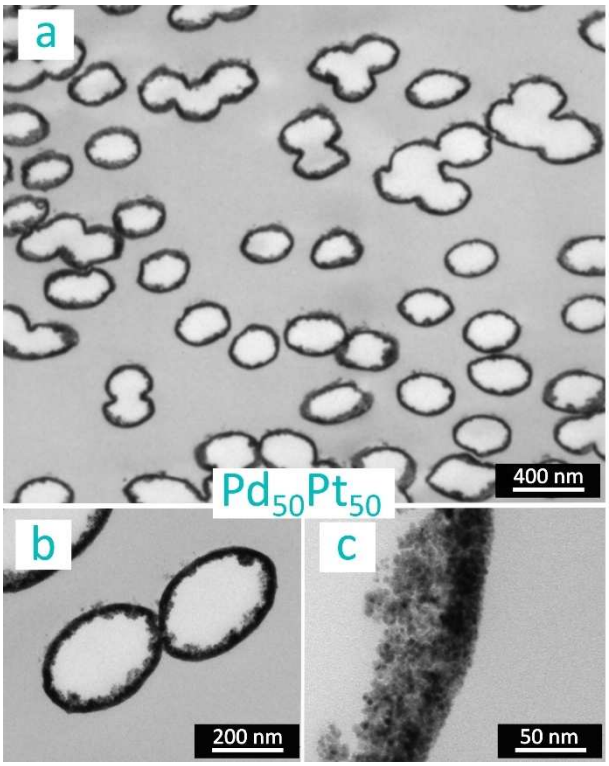

Figure 4. TEM-images of the $Pd_{50}Pt_{50}$-NTs at varied magnifications.

through two directly neighboring $Pd_{50}Pt_{50}$ NTs. At high magnifications, the efficient coverage of the template's nanochannel wall by a dense, tight-fitting nanoparticle film is apparent (Figure 4(c)), evidencing the high density of nucleation sites provided by template activation, and the efficient structural replication by the plating reaction. The average particle size in the shown NT wall of ~50 nm thickness is 10 nm ± 5 nm (Figure 4c). The NTs remained intact through microtome cutting, demonstrating the coherence of the deposited nanoparticle films.

In order to elucidate the phase composition of the Pd–Pt NTNWs and clarify whether the metals are present in alloyed or segregated form, we performed XRD on three selected samples ($Pd_{100}Pt_0$, $Pd_{50}Pt_{50}$ and Pd_0Pt_{100}). Due to the intricacies associated with our system (similar lattice parameters of Pd and Pt, distinct reflex broadening due to the small size of the NPs), the analysis was complemented by Rietveld refinement (Figure 5).

Each pattern can be indexed with a single cubic phase with the space group $Fm\bar{3}m$, which is in agreement with for the fcc structure of the pure metals (a_{Pd} = 3.89 Å and a_{Pt} = 3.92 Å).[60,61] However, when applying a single phase to fit the pattern, we observed considerable misfits regarding the asymmetry of the reflections with extended tails towards lower angles. The fundamental approach used for the data analysis shows that this asymmetry must relate to the sample,[62] and does not originate from the geometry of the diffraction setup (e.g. axial beam divergence). For metals, such asymmetry could originate from strain effects within the samples, e.g. due to the geometric confinement within the template. In order to fit the

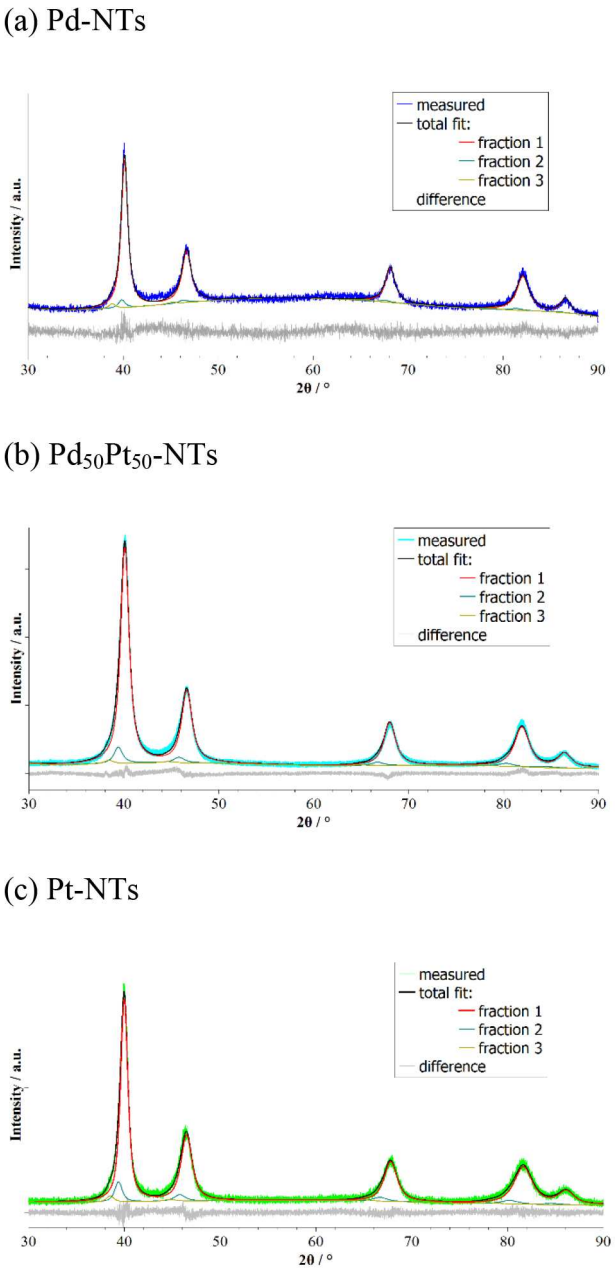

Figure 5. XRD pattern and Rietveld refinement fits for the three different NT-compositions: (a) pure Pd, (b) $Pd_{50}Pt_{50}$, (c) pure Pt.

patterns appropriately, an anisotropic strain broadening after Stephen was included to account for the anisotropic reflection broadening.[62] The asymmetry was modelled by using three metal phases with different lattice parameters, but identical symmetry dependent broadening parameters. The model allows two independent anisotropic strain parameters for SHKL, namely S400 and S220, which were constrained to be equal for each fraction. For the samples, a crystallite size of a few nm was found. A quantification of the elemental ratio of the bimetallic NT sample was determined from the weighted lattice parameters of the three samples [Eq. (8)]:

$$x_{Pd} = \frac{a_{Pt} - a_{PdPt}}{a_{Pt} - a_{Pd}} \cdot 100 \quad (8)$$

Where the weighted lattice parameter of each sample was determined according to Equation (9):

$$a_i = \frac{\sum_{n=1}^{3}(a_j s_j)}{\sum_{n=1}^{3}(s_j)} \quad (9)$$

With j being the type of sample (Pt, Pd, or PdPt), n the number of fractions which had to be used to fit the asymmetry of the reflections, and a_j/s_j being the lattice parameter and weight fractions of each fraction. Based on this fit, we found a Pd content of ~57 at.%, which is similar to the EDX results, corroborating the approximate 1:1-ratio of the metals in this material as well as the formation of bimetallic alloy phases in the nanomaterial. Probably, a variety of bimetallic phases are present that slightly differ in their atomic Pd/Pt-ratios, resulting in a respective distribution of lattice parameters (Table 1). From a synthetic point of view, Pd-rich phases could be formed during the activation process and during the early stages of plating, which occur on Pd seeds. Also, locally fluctuating Pd and Pt concentrations during plating could explain differing Pd/Pt-ratios within the nanoscopic phases.

XPS was used to determine the NT's surface speciation of three samples, $Pd_{100}Pt_0$, $Pd_{50}Pt_{50}$, Pd_0Pt_{100} (Figure 6). As the NTNWs are 3D negatives of the utilized template, the seeds stemming from the activation process remain on the outer NT surface after template dissolution. Therefore, they are in the focus of the surface-sensitive XPS method. The elemental composition of the samples is in good agreement with the synthetic expectations. There are traces of surficial Pd on the monometallic Pt NTs, arising from the activation step of the seeding procedure. In comparison, the monometallic Pd NTs never came in contact with Pt during synthesis, thus no signs of Pt are found. Residues of Sn stemming from the sensitization step were present on all of the NTs' outer surfaces.[1,2,8,29] Varying amounts of O, C and In are present as well, which can be attributed to polymer residues (C, O) and the sample preparation (adsorbed atmospheric contaminations containing C, O, In foil for embedding the NTNWs).

Table 1. Fit parameters for each set of data and structure fractions.

	j	Fractions [wt.%]	Lattice parameter [Å]	Crystallite size [nm]	GOF	Eta	S400	S220
Pd	1	92.22 ± 4.29	3.895 ± 0.0009	7.62 ± 3.25	1.10	0.68 ± 0.18	14595 ± 6070	-18835 ± 7741
	2	4.84 ± 4.41	3.923 ± 0.0115					
	3	2.94 ± 0.34	4.021 ± 0.0042					
Pt	1	88.42 ± 0.62	3.910 ± 0.0004	19.60 ± 1.30	1.08	0.68 ± 0.02	143248 ± 3658	451001 ± 5778
	2	8.70 ± 0.62	3.971 ± 0.0026					
	3	2.88 ± 0.15	4.058 ± 0.0027					
$Pd_{50}Pt_{50}$	1	91.77 ± 0.27	3.903 ± 0.0002	7.08 ± 0.12	1.91	0.64 ± 0.03	22289 ± 1140	-1331 ± 1349
	2	6.96 ± 0.27	3.969 ± 0.001					
	3	1.26 ± 0.06	4.069 ± 0.002					

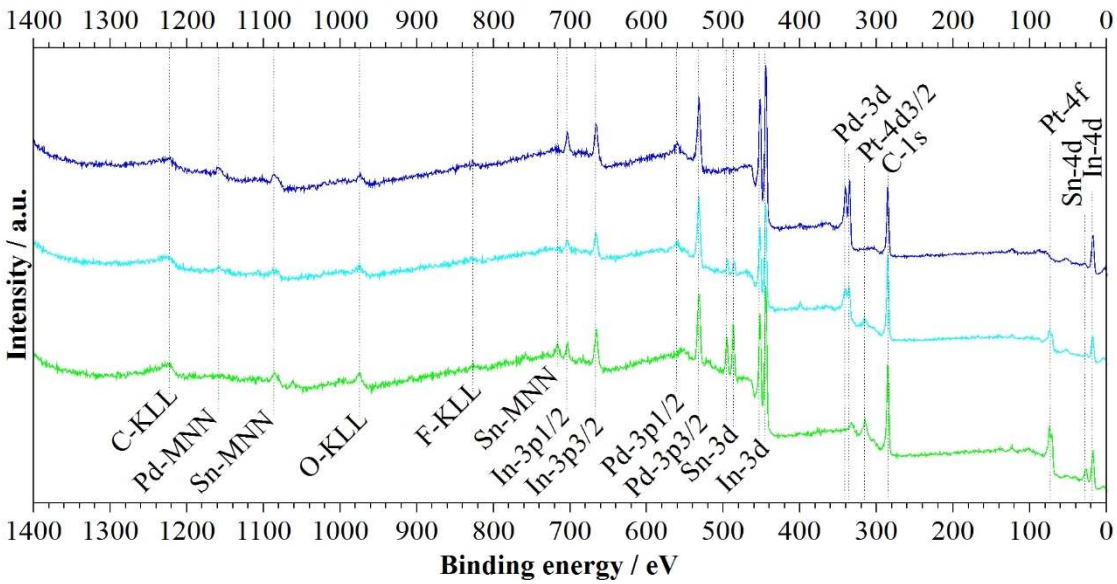

Figure 6. Survey XP-spectra: Pd-NTs (blue); $Pd_{50}Pt_{50}$-NTs (cyan); Pt-NTs (green).

2.3. Tailoring the Composition of Pd/Pt-NT Catalysts for Methanol Oxidation

The Pd_xPt_y NTNWs' catalytic activity regarding methanol oxidation was investigated using cyclovoltammetry (CV). For the purpose of finding the optimal NT composition, seven samples of varying Pd/Pt-ratios were characterized. First, the electrochemical active surface area (ECSA) was determined in sulfuric acid (see "Supporting Information"), using the average charge density value of 210 $\mu C\,cm^{-2}$ for one complete monolayer of adsorbed H on Pt.[63–65] Pd can not only bind H by adsorption, but also absorb it, complicating an exact surface determination via H-monolayer-desorption charges in the case of Pd-containing samples. Due to the tendency to bind larger amounts of H, this method tends to yield too large surface area values. By neglecting the H-absorption of Pd and assuming its H-adsorption charge density value of 210 $\mu C\,cm^{-2}$, equal to that of Pt,[41–43,63] the resulting ECSAs are generally overestimated. Another method for determining the ECSA of Pd and Pt catalysts is integrating the charge of the surface-oxide reduction region. The charge values associated with the reduction of one monolayer of PdO and PtO are 424 $\mu C\,cm^{-2}$ and 420 $\mu C\,cm^{-2}$, respectively.[63] Being more error-prone, this approach is not as commonly used for the ECSA determination of Pt. To estimate the degree of surface area exaggeration in our bimetallic NTs by using H desorption, we apply both ECSA-determining methods in this work for comparison (see the Supporting Information: A_H and A_O for the calculated ECSA-values by the respective method). As it turns out, an overestimation of ECSAs resulting from neglecting the H-absorption of Pd is noticeable for NTNWs with a Pd content of 50% and higher. The Pt-rich samples (Pt-content $>50\%$) show good agreement of the ECSA values calculated with both methods. Importantly, we can rule out that the error introduced in the case of high Pd contents shifts the activity order of our different catalysts (see below). Due to the ability to reliably characterize the ECSA of our more active, Pt-rich catalysts, we use the H-normalized values in our discussion below.

Upon addition of methanol to the electrolyte, broad oxidation peaks appear at $E \approx 1$ V in the forward scan (Figure 7). The maximum peak current densities (pcd) and the shifts of the corresponding potentials E_r at recurring potential depend heavily on the catalyst composition. As measure for the activity of the respective samples, the pcd values of the anodic scan are used. Another method for the comparison of catalytic performance is the methanol oxidation current at recurring potential. However, this parameter is error-prone, because the oxide reduction is strongly dependent on the nobility of the respective catalyst and therefore dependent on its Pd/Pt-ratio, as well as on the cycling conditions.[63–65] The oxidized surface of Pd-rich samples is reduced at such low potentials, that hardly any driving force for methanol oxidation is present, resulting in much lower pcd values at recurring potentials for Pd-rich samples in comparison to Pt-rich samples.[5]

The monometallic Pd-NTs show the lowest activity in methanol oxidation with a corresponding. With increasing Pt content, the activity of the bimetallic NTNWs increases until a pcd maximum is reached for the $Pd_{20}Pt_{80}$-NTs (226 $\mu A\,cm^{-2}$) which then descends again to 108 $\mu A\,cm^{-2}$ for the pure Pt NTNW. Figure 8 shows that, independent of the surface area normalization, the $Pd_{80}Pt_{20}$ NTNW shows the highest pcd and therefore the best catalytic activity.

The considerable increase in the oxidation current density when substituting 20–30 at.% Pt with Pd could be attributed to different mechanisms:

First, alloying Pt with Pd could facilitate the reduction of oxide species: The characteristic value E_r in the cathodic scan is shifted to more positive values with increasing Pd-contents for Pd-contents below 50%. This indicates that the formation of inactive metal oxides is impeded.

Second, the presence of Pd can result in electronic changes which can weaken the degree of Pt poisoning: Through alloying with Pd, the Fermi-level of the solid shifts downwards, reducing the occupation of the Pt 4d orbitals responsible for forming the strong Pt–CO-backbond.[24,25]

Third, a catalytic synergy between Pd and Pt could arise from the bifunctionality of Pt–Pd ensembles: Pd is an efficient promoter for OH_{ads} formation,[25] which boosts the oxidation of CO_{ads} on neighboring Pt triplet site representing the active centers for methanol oxidation. Due to the higher intrinsic activity of Pt as compared to Pd in the methanol oxidation, it is anticipated that optimal surface compositions contain just enough Pd to reliably ensure the direct proximity of Pd to Pt-triplet ensemble sites capable of oxidizing methanol, and

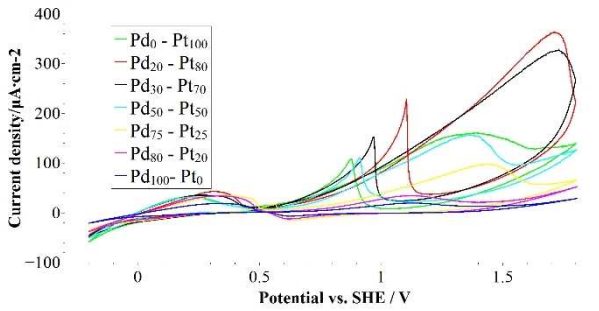

Figure 7. CVs of all seven investigated NTNW-samples in 0.5 M H_2SO_4 + 1.2 M methanol. All currents were normalized by the ECSA values calculated by H desorption.

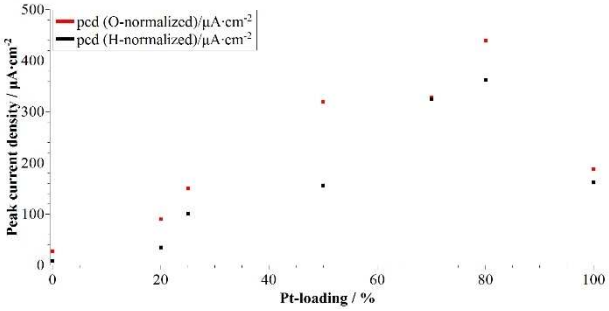

Figure 8. Measured peak current densities over Pt-content for all seven investigated samples.

benefit from a considerable Pt excess (up to 90%),[43] like in our case.

In accordance with all three key aspects above, within our sample size, the $Pd_{20}Pt_{80}$ catalyst showed the quickest stripping of surface oxides in the cathodic scan (E_r) and the highest pcd in methanol oxidation. Our experimentally determined optimum composition is close to the value expected for a solid solution catalyst benefiting maximizing bifunctional effects while maintaining a high density of Pt triplet sites.

Building up on the fact, that sample $Pd_{20}Pt_{80}$ showed the quickest stripping of surface oxides, we conducted a CO-stripping experiment after 1 h of indirect poisoning with potentiostatic application in 0.1 M formic acid (HCOOH). Similar to a recent study in our research group,[53] our experiment compares the CO-stripping capabilities of our $Pd_{20}Pt_{80}$ NTNW to the pure Pt NTNW (Pd_0Pt_{100}). The plotted results can be seen in Figure 9 of the Supporting Information. The $Pd_{20}Pt_{80}$ sample shows improved CO-stripping capability compared to the pure Pt NTNW: The CO-stripping off the Pt NTNW is located at 500 mV, whereas the $Pd_{20}Pt_{80}$ sample shows a shift of the CO-stripping to lower potentials reaching maximum currents at 445 mV.

In previous studies, compared to carbon-supported metal nanoparticle catalysts, metallic nanotube have shown to be less prone to typical degradation mechanisms such as support corrosion, nanoparticle detachment, or dissolution.[1,2] To investigate the stability of our catalysts, we performed accelerated aging studies using the most active $Pd_{20}Pt_{80}$ nanotubes and the Pd_0Pt_{100} nanotubes, and comparing them with commercial Pt–C. The results from the long term cycling CVs are shown in Figure 9: Over 300 recorded cycles, the commercial sample Pt black loses almost its entire ECSA, decreasing it to 1% (black line). In comparison, the Pd_0Pt_{100} (green line) retains 46% of its initial ECSA after 300 cycles and thus showing better stability than the commercial Pt black. This difference is notable in the first 150 cycles of the measurement. The $Pd_{20}Pt_{80}$ exhibits the best stability of the three investigated samples, retaining 96% of its initial ECSA. Because the $Pd_{20}Pt_{80}$ NTNW did not significantly lose ECSA in comparison to the pure Pt NTNW we hypothesize that compositional effects between Pd and Pt are causing the superior stability of the alloy catalyst. In addition to that, the CO-stripping experiments show evidence that these synergistic effects are accompanied by better CO-stripping capabilities. Furthermore, we conclude that the nanostructured hollow architecture causes the better stability of the Pd_0Pt_{100} NTNW compared to Pt black.

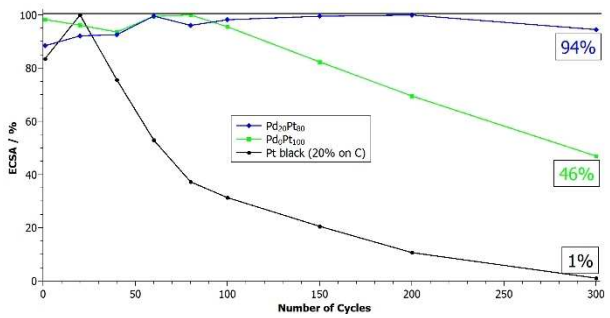

Figure 9. Long-term study (300 cycles in 0.5 M H2SO4) with samples Pd20Pt80, Pd0Pt100 and the commercial catalyst Pt black (20% Pt on C). The respective ESCAs were evaluated for cycle 1, 20, 40, 60, 80, 100, 150, 200, 300

3. Conclusions

Bimetallic Pd_xPt_y nanofilms covering the whole composition spectrum were synthesized with electroless plating. Key for achieving alloy plating was the development of mutually compatible plating baths for the individual metals, which both share the same reducing agent, employ non-interfering ligands, can be operated at the same pH and temperature, and result in similar Pt and Pd deposition rates. Due to the excellent conformity and nanoscale homogeneity of the deposit, we could replicate the intricate inner surface structure of ion-track etched polycarbonate membranes, enabling the production of free-standing Pd_xPt_y NTNWs of arbitrary composition. Using the electro-oxidation of methanol as a model reaction, we have shown how the compositional freedom provided by our synthesis route can be used to optimize the material performance in selected applications. The highest surface normalized activity was found for the $Pd_{20}Pt_{80}$ NTNW, reaching a pcd of 0.363 mA cm^{-2} – which represents more than a two-fold increase in comparison to pure Pt NTNWs. CO-stripping experiments show evidence for a superior CO-stripping capability of the $Pd_{20}Pt_{80}$ NTNW compared to the pure Pt NTNW. Long term cycling experiments prove the better ageing resistance of the $Pd_{20}Pt_{80}$ NTNW compared to the pure Pt NTNW, both samples outperforming the commercial catalyst Pt black.

The outlined reactions can be applied to different template materials and shapes and hence, be coupled with other synthetic approaches, e.g. sequential deposition or derivatization reactions to produce more complex materials. Our general strategy represents a starting point for developing other electroless alloy plating reactions.

Experimental Section

General procedures and chemicals

Laboratory glassware was cleaned with aqua regia. All procedures were performed with ultrapure water (R > 18 MΩ cm^{-1}, Millipore). The following chemicals have been used as received: 4-dimethylaminopyridine (DMAP, Fluka, ≥99.0%), dichloromethane (Merck, ≥99.8%), ethylenediaminetetraacetic acid (EDTA, Sigma-Aldrich, ≥99.0%), ethanol (absolute, Labor Service GmbH, p.a.), ethylenediamine (en, Fluka, puriss. p.a.), formic acid (HCOOH, ≥95%, Sigma-Aldrich), hexachloroplatinic acid (Fluka, 8% in dil. HCl), hydrazine monohydrate (Merck, 80% in H_2O), KCl (Sigma, ≥99.0%), methanol (AppliChem Panreac, 99.5%), methanol (Labor Service GmbH, for analysis; used for catalysis), Nafion (5% in ethanol, Electrochem, Inc.) $PdCl_2$ (Alfa Aesar, 99.9%), Pt black (20% nominally on C, Alfa Aesar), sulfuric acid (volumetr. Solution, AppliChem Panreac, 0.5 M), trifluoroacetic acid (TFA, Sigma-Aldrich, 99%), $SnCl_2$ dihydrate (Sigma-Aldrich, 98%).

Template seeding

Polycarbonate membranes (Whatman, nominal thickness 20 μm, pore density: 1.5×10^8 cm^{-2}, pore diameter: 400 nm) show interconnectivity of the nanochannels, which results from angled ion irradiation, allowing the formation of free-standing nano-networks by pore replication.[1] Prior to plating, the polymer templates are covered with Pd nanoparticle seeds. This is achieved by first immersing the templates in a methanolic solution of Sn(II) (42 mM $SnCl_2$, 71.4 mM TFA, for 15 min), followed by immersion in an aqueous solution of Pd(II) (11 mM $PdCl_2$, 33 mM KCl, for 5 min). Between transfers the template is rinsed with ethanol to avoid mixing of the utilized solutions. This activation procedure is repeated three times. The final template shows a brown color resulting from Pd NPs covering the template's surface including the pores.

Electroless plating

The plating baths consist of two components: The first component (a) contains the metal source, complexing agents, chemicals for pH adjustment and/or capping agents. The second component (b) contains the reducing agent hydrazine and is mixed with the former in a 1:1 ratio by volume. The electroless Pd plating consists of the following combined solutions (a_1) and (b_1): (a_1) $PdCl_2$ (4.2 mM), EDTA (15.4 mM), dimethylaminopyridine (DMAP, 20.5 mM); (b_1) hydrazine (44.6 mM). The electroless Pt plating consists of the following solutions (a_2) and (b_2): (a_2) H_2PtCl_6 (3.5 mM), ethylendiamine (en, 36.4 mM); (b_2) hydrazine (257.1 mM). Plating is performed by combining both solutions (a) and (b) at 70–80 °C and adding a seeded/activated template under stirring. Alloy plating baths are produced by mixing the monometallic variants in different ratios. After 2–3 h, the template color changes to black, indicating metallization. With ongoing plating and growing film thickness, a shiny, smooth surface film will appear on top of the template, indicating the end point of the synthesis. The plating baths should show a faded yellow color (due to the depletion of the Pd and Pt complexes) and no other precipitation within the glassware except on the previously activated template.

Characterization

Secondary electron microscopy (SEM) with integrated energy-dispersive X-ray analysis (EDX). The measurements were performed on template-freed NTs, which were obtained by dissolving the polymer with dichloromethane and collected on Si wafer pieces. Imaging was performed with a Philips XL30 FEG using acceleration voltages of 10–30 kV, and accompanied by EDX analysis using an EDAX Genesis spectrometer.

X-ray diffraction analysis (XRD). The general XRD measurements (Θ-2Θ scans) were performed with a Seifert PTS 3003 diffractometer using a Cu anode, an X-ray mirror installed on the primary side, and a long Soller-slit and graphite monochromator built in on the secondary side to separate the Cu K_α-line (40 kV/40 mA).

Rietveld-refinement. Detailed diffractograms were recorded in a Bruker D8 diffractometer with Bragg-Brentano geometry and a Cu anode (Cu-$K_{\alpha1,2}$-radiation at 30 kV/40 mA) using a VANTEC detector (3° detector opening). Data were recorded for an angular range from 10–90° 2θ with a step size of ~0.007°. A fixed divergence slit with a 6 mm opening was used. A total measurement time of 3 to 7 h was chosen for this angular range, whereas longer measurement times were used for samples with reduced amount of available powder to obtain comparable signal-to-noise ratios. The obtained data were fitted using the Rietveld method as implemented in the software TOPAS 6 (Bruker AXS, Karlsruhe, Germany). The instrumental intensity function was determined empirically from a fundamental parameters set by utilizing a reference scan of a LaB_6 standard (NIST 660a).[60]

X-ray photoelectron spectroscopy (XPS). The XPS measurements were carried out on the DAISY-MAT, a Physical Electronics PHI 5700 multitechnique surface analysis system, using the monochromated Al-K_α-line with $h_{n=}$1486.6 eV as X-ray radiation, with a pass energy of 187.85 eV (survey spectra). An Ag-standard was used for calibration (Ag3$d_{5/2}$ and Fermi level).

Transmission electron microscopy (TEM). The TEM measurements were executed with a CM20 microscope (FEI, Eindhoven, The Netherlands, 200 kV acceleration voltage, LaB_6 cathode): The nanostructure-containing templates were embedded in Araldite 502 (polymerization at 60 °C for 16 h) and examined as ultrathin sections (70 nm thickness, Ultracut E ultramicrotome (Reichert-Jung) equipped with a diamond knife (DKK)).

Cyclic voltammetry measurements (CV). CV measurements were conducted with a Gamry 600 potentiostat using a three-electrode setup comprising a reference electrode ($Hg|Hg_2SO_4+0.682$ V vs. standard hydrogen electrode (SHE), $Ag|AgCl+0.210$ V vs SHE), a Pt-mesh counter electrode and a polished glassy carbon working electrode (3 mm diameter). Comparable amounts of NT catalysts were drop coated on the working electrode in the form of dichloromethane suspensions: An eighth of a plated template was dissolved in dichloromethane and 50 μl of this suspension was drop coated onto the working electrode. A thermostat was used to adjust the temperature to 25 °C. Prior to the experiments which were conducted under N_2 stream, the electrolytes were purged with N_2 for 5 min. The conditions (electrolyte, scan rate, reference electrode) for all CV experiments are summarized in Table 3 of the Supporting Information. The Pt black sample was prepared using 15 mg of powder, dissolving it in 1 mL of a 1:1 water + Nafion (5% in ethanol) solution. For one sample preparation 5 μL were drop coated onto the working electrode and dried for 10 min at 100 °C.

Acknowledgements

This work was supported by the German Federal Ministry of Education and Research under the acronym "HI-EXE" as part-project 6 (Prof. Ensinger) of "Forschungsverbund Ionenstrahl-induzierte Materialveränderungen" under contract number "05K16RDC".

Conflict of Interest

The authors declare no conflict of interest.

Keywords: nanotube network · Pd–Pt alloy · electroless plating · heterogeneous catalysis

[1] T. Walbert, M. Antoni, F. Muench, T. Späth, W. Ensinger, *ChemElectroChem* **2018**, *5*, 1–12.
[2] F. Muench, *Catalysts* **2018**, *8*, 597.
[3] J. Ge, P. Wei, G. Wu, Y. Liu, T. Yuan, Z. Li, Y. Qu, Y. Wu, H. Li, Z. Zhuang, X. Hong, Y. Li, *Angew. Chem.* **2018**, *130*, 3493–3496; *Angew. Chem. Int. Ed.* **2018**, *57*, 3435–3438.
[4] H. Hu, Z. Jiao, J. Ye, G. Lu, Y. Bi, *Nano Energy* **2014**, *8*, 103–109.

[5] F. Muench, S. Kaserer, U. Kunz, I. Svoboda, J. Brötz, S. Lauterbach, H.-J. Kleebe, C. Roth, W. Ensinger, *J. Mater. Chem.* **2011**, *21*, 6286–6291.
[6] Z. Li, *Colloids Surf. A: Physicochem. Eng. Aspects* **2015**, *464*, 129–133.
[7] F. Muench, M. Oezaslan, I. Svoboda, W. Ensinger, *Mater. Res. Express* **2015**, *2*, 105010.
[8] I. V. Korolkov, A. A. Mashentseva, O. Güven, Y. G. Gorin, A. L. Kozlovskiy, M. V. Zdorovets, I. S. Zhidkov, S. O. Cholach, *Mater. Chem. Phys.* **2018**, *217*, 31.
[9] Y. Bi, G. Lu, *Electrochem. Commun.* **2009**, *11*, 45–49.
[10] H. M. Chen, C. F. Hsin, R.-S. Liu, J.-F. Lee, L.-Y. Jang, *J. Phys. Chem. C* **2008**, *112*, 7522–7526.
[11] Z. Chen, M. Waje, W. Li, Y. Yan, *Angew. Chem. Int. Ed.* **2007**, *46*, 4060–4063.
[12] F. Muench, E.-M. Felix, M. Rauber, S. Schäfer, M. Antoni, U. Kunz, H.-J. Kleebe, C. Trautmann, W. Ensinger, *Colloids Surf. A: Physicochem. Eng. Aspects* **2016**, *508*, 197–204.
[13] M. Stano, S. Schäfer, A. Wartelle, M. Rioult, R. Belkhou, A. Sala, T. O. Menteş, A. Locatelli, L. Cagnon, B. Trapp, S. Bochmann, S. Martin, E. Gautier, J. C. Toussaint, W. Ensinger, O. Fruchart, *SciPost Phys.* **2018**, *5*, 038.
[14] Y. L. Li, S. L. Tanga, R. Xie, Y. Wang, M. Yang, J. L. Gao, W. B. Xia, Y. W. Du, *Appl. Phys. Lett.* **2012**, *100*, 052402.
[15] S.-W. Lee, M. Jafary-Zadeh, D. Z. Chen, Y.-W. Zhang, J. R. Greer, *Nano Lett.* **2015**, *15*, 5673–5681.
[16] S. Ye, G. Marston, J. R. McLaughlan, D. O. Sigle, N. Ingram, S. Freear, J. J. Baumberg, R. J. Bushby, A. F. Markham, K. Critchley, P. L. Coletta, S. D. Evans, *Adv. Funct. Mater.* **2015**, *25*, 2117–2127.
[17] S. Zhang, Y. Shao, H.-G. Liao, J. Liu, I. A. Aksay, G. Yin, Y. Lin, *J. Phys. Chem. C* **2012**, *116*, 18093–18100.
[18] H. Wang, C.-W. Xu, F. Cheng, M. Zhang, S. Wang, S. P. Jiang, *Electrochem. Commun.* **2008**, *10*, 1575–1578.
[19] Q. Yuan, Z. Zhou, J. Zhuang, X. Wang, *Chem. Commun.* **2010**, *46*, 1491–1493.
[20] S. Y. Tee, E. Ye, P. H. Pan, C. J. J. Lee, H. K. Hui, S.-Y. Zhang, L. D. Koh, Z. Dongc, M.-Y. Han, *Nanoscale* **2015**, *7*, 11190–11198.
[21] S. M. Kim, L. Liu, S. H. Cho, H. Y. Jang, S. Park, *J. Mater. Chem. A* **2013**, *1*, 15252.
[22] A. B. Yousaf, M. Imran, N. Uwitonze, A. Zeb, S. J. Zaidi, T. M. Ansari, G. Yasmee, S. Manzoo, *J. Phys. Chem. C* **2017**, *121*, 2069–2079.
[23] N. S. Porter, H. Wu, Z. Quan, J. Fang, *Acc. Chem. Res.* **2013**, *46*, 1867–1877.
[24] Y. Liu, M. Chi, V. Mazumder, K. L. More, S. Soled, J. D. Henao, S. Sun, *Chem. Mater.* **2011**, *23*, 4199–4203.
[25] G. You, J. Jiang, M. Li, L. Li, D. Tang, J. Zhang, X. C. Zeng, R. He, *ACS Catal.* **2018**, *8*, 132–143.
[26] L. Liu, S.-H. Yoo, S. A. Lee, S. Park, *Nano Lett.* **2011**, *11*, 3979–3982.
[27] M. N. Nadagouda, V. Polshettiwara, R. S. Varma, *J. Mater. Chem.* **2009**, *19*, 2026.
[28] C. H. Kim, J. Y. Han, H. Lim, K. Y. Lee, S. K. Ryi, *J. Membr. Sci.* **2018**, *563*, 75.
[29] S. Schaefer, E.-M. Felix, F. Muench, M. Antoni, C. Lohaus, J. Brötz, U. Kunz, I. Gärtner, W. Ensinger, RSC Adv. 2016, 6, 70033–70039.
[30] Y. Kim, H. J. Kim, Y. S. Kim, S. M. Choi, M. H. Seo, W. B. Kim, *J. Phys. Chem. C* **2012**, *116*, 34, 18093–18100.
[31] F. Muench, D. M. De Carolis, E.-M. Felix, J. Brötz, U. Kunz, H.-J. Kleebe, S. Ayata, C. Trautmann, W. Ensinger, *ChemPlusChem* **2015**, *80*, 1448–1456.
[32] F. Zhan, T. Bian, W. Zhao, H. Zhang, M. Jin, D. Yang, *CrystEngComm* **2014**, *16*, 2411–2416.
[33] S. Guo, S. Dong, E. Wang, *ACS Nano* **2010**, *4*, 1, 547–555.
[34] M. Arenz, V. Stamenkovic, T. J. Schmidt, K. Wandelt, P. N. Ross, N. M. Markovic, *Phys. Chem. Chem. Phys.* **2003**, *5*, 4242–4251.
[35] T. Boettcher, S. Schaefer, M. Antoni, T. Stohr, U. Kunz, M. Dürrschnabel, L. Molina-Luna, W. Ensinger, F. Muench, *Langmuir* **2019**, *35*, 4246–4253.
[36] F. Muench, U. Kunz, H. F. Wardenga, H.-J. Kleebe, W. Ensinger, *Langmuir* **2014**, *30*, 10878–10885.
[37] A. A. Mashentseva, M. V. Zdorovets, *Petrol. Chem.* **2019**, *59*, 552–557.
[38] J. Duan, J. Liu, Y. Zhang, C. Trautmann, D. Y. Lei, *J. Mater. Chem. C* **2016**, *4*, 3956.
[39] W. Liu, P. Rodriguez, L. Borchardt, A. Foelske, J. Yuan, A.-K. Herrmann, D. Geiger, Z. Zheng, S. Kaskel, N. Gaponik, R. Kötz, T. J. Schmidt, A. Eychmüller, *Angew. Chem. Int. Ed.* **2013**, *52*, 9849–9852; *Angew. Chem.* **2013**, *125*, 10033–10037.
[40] C. R. K. Rao, D. C. Trivedi, *Coord. Chem. Rev.* **2005**, *249*, Issues 5–6, 613–631.
[41] K. C. Neyerlina, R. Srivastavaa, C. Yua, P. Strasser, *J. Power Sources* **2014**, *268*, 712–717.
[42] H. A. Gasteiger, N. Markovic, P. N. Ross Jr., E. J. Cairns, *J. Phys. Chem.* **1993**, *97*, 12020–12029.
[43] M. A. Matin, J.-H. Jang, E. Lee, Y.-U. Kwon, *J. Appl. Electrochem.* **2012**, *42*, 827.
[44] B. Kakade, I. Patil, M. Lokanathan, A. Swami, *J. Mater. Chem. A* **2015**, *3*, 17771–17779.
[45] D. Liang, W. Shao, G. Zangari, *J. Electrochem. Soc.* **2016**, *163*, D40–D48.
[46] D. Liang, G. Zangari, *Langmuir* **2014**, *30*, 2566–2570.
[47] D. Liang, P. Rajput, J. Zegenhagen, G. Zangari, *ChemElectroChem* **2014**, *1*, 787–792.
[48] F. Muench, A. Solomonov, T. Bendikov, L. Molina-Luna, I. Rubinstein, A. Vaskevich, *ACS Appl. Biomater.* **2019**, *2*, 856–864.
[49] A. Wongkaew, Y. Zhang, J. M. M. Tengco, D. A. Blom, P. K. Sivasubramanian, P. T. Fanson, J. R. Regalbuto, J. R. Monnier, *Appl. Catal. B: Env.* **2016**, *188*, 367–375.
[50] W. Diao, J. M. M. Tengco, J. R. Regalbuto, J. R. Monnier, *ACS Catal.* **2015**, *5*, 5123–5134.
[51] T. R. Garrick, W. Diao, J. M. Tengco, E. A. Stach, S. D. Senanayake, D. A. Chen, J. R. Monnier, J. W. Weidner, *Electrochim. Acta* **2016**, *195*, 106–111.
[52] R. J. Nichols, *J. Sci. Ind. Res.* **2003**, *62*, 97–105.
[53] F. Muench, G. A. El-Nagar, T. Tichter, A. Zintler, U. Kunz, L. Molina-Luna, V. Sikolenko, C. Pasquini, I. Lauermann, C. Roth, *ACS Appl. Mater. Interfaces* **2019**, *11*, 46, 43081–43092.
[54] W. M. Haynes, *Handbook of Chemistry and Physics*, CRC Press **2016**, 93.
[55] G. Milazzo, S. Caroli, R. D. Braun, *Tables of Standard Electrode Potentials*, Electrochem. Soc. **1978**, 261 C–261 C.
[56] A. J. Bard, *Standard Potentials in Aqueous Solutions*, Routledge **2017**.
[57] Y.-J. Chao, C.-R. Liu, L.-S. Pan, C.-L. Lee, *Electrochim. Acta* **2015**, *183*, C, 20–26.
[58] R. Gilliam, S. Thorpe, D. Kirk, *J. Appl. Electrochem.* **2007**, *37*, 233–239.
[59] F. Muench, S. Lauterbach, H.-J. Kleebe, W. Ensinger, *e-J. Surf. Sci. Nanotechnol.* **2012**, *10*, 578–584.
[60] PDF-2 card: Pd (fcc) 46–1043 (Seifert Analyze): Kern, A., Eysel, W., Mineralogisch-Petrograph. Inst., Univ. Heidelberg, Germany, 00GRNT, **1993**.
[61] PDF-2 card: Pt (fcc) 1–1194 (Seifert Analyze): Hanawalt, *ANCHAM* **1938**, *10*, 475.
[62] R. W. Cheary, A. A. Coelho, J. P. Cline, *J. Res. Natl. Inst. Stand. Technol.* **2004**, *109*, 1–25.
[63] M. Shao, J. H. Odell, S.-I. Choi, Y. Xia, *Electrochem. Commun.* **2013**, *31*, 46–48.
[64] D. Zhan, J. Velmurugan, M. V. Mirkin, *J. ACS* **2009**, *131*, 14756–14760.
[65] M. Łukaszewski, M. Soszko, A. Czerwiński, *Int. J. Electrochem. Sci.* **2016**, 4442–4469.
[66] K. C. Neyerlina, R. Srivastavaa, C. Yua, P. Strasser, *J. Power Sources* **2014**, *268*, 712–717.
[67] D. Y. Chung, K.-J. Lee, Y.-E. Sung, *J. Phys. Chem. C* **2016**, *120*, 9028–9035.

Manuscript received: November 18, 2019
Revised manuscript received: December 26, 2019
Accepted manuscript online: January 10, 2020